ChemElectroChem | doi.org/10.1002/celc.202000181

European Chemical Societies Publishing

Comparing the Performance of Nb_2O_5 Composites with Reduced Graphene Oxide and Amorphous Carbon in Li- and Na-Ion Electrochemical Storage Devices**

Xianying Han,[a] Patrícia A. Russo,*[a] Claudia Triolo,[b] Saveria Santangelo,[b] Nicolas Goubard-Bretesché,[a] and Nicola Pinna*[a]

Two-dimensional (2D) reduced graphene oxide (rGO) is often combined with metal oxides for energy-storage applications, owing to its unique properties. Here, we compare the electrochemical performance of Nb_2O_5-rGO and amorphous carbon-coated-Nb_2O_5 composites, synthesized in similar conditions. The composite made of Nb_2O_5 and amorphous carbon (using 1,3,5-triphenylbenzene as carbon source) outperforms the Nb_2O_5-rGO counterpart as a high rate anode electrode material in Li-ion and Na-ion half-cells and hybrid supercapacitors, delivering specific capacities of 134 mAh g^{-1} at 25 C against 98 mAh g^{-1} for the rGO-based composite (in Li electrolyte) and 125 mAh g^{-1} at 20 C against 98 mAh g^{-1} (in Na electrolyte). The organic molecules, which are the precursor of the amorphous carbon, control the size and coat the metal oxide particles more efficiently, leading to more extensive carbon-oxide contacts, which benefits the energy-storage performance.

1. Introduction

Energy-storage devices with higher energy and power densities than those currently available are needed to match the future energy demands of society.[1] To address this challenge, devices such as lithium-ion batteries, sodium-ion batteries, or hybrid supercapacitors (HSCs), are being intensively investigated.[2–3] The active electrode materials are crucial for the development of efficient energy-storage systems and, in particular, materials displaying high C-rate capacity are necessary to achieve simultaneously high energy and power densities.[4–5]

Orthorhombic niobium pentoxide (T-Nb_2O_5) is a promising anode material for Li-ion storage systems, due to its high theoretical capacity (~200 mAh g^{-1}), broad voltage operation window and high C-rate capability.[6] The charge is stored through an intercalation pseudocapacitance mechanism, as the orthorhombic structure contains sufficiently large channels for fast lithium-ion insertion/deinsertion to/from the structure to occur without structural modifications, which can lead to high C-rate capability and stability.[4,6–7] Nevertheless, the low electrical conductivity of T-Nb_2O_5 still limits the ion/electron transport and thus the electrochemical performance.[8] The effect is more pronounced in sodium electrolytes, where the electrochemical performance of pure Nb_2O_5 is poor and dependent on the surface area.[7] This is due to the larger size of the sodium ion compared to lithium that leads to significant slower kinetics, lower capacity and quicker capacity fading as the C-rate increases.[9] Although more demanding in terms of active materials, Na-ion energy storage devices are desirable owing to sodium being less expensive and more abundant than lithium.[10–12] Consequently, recently efforts have been devoted to the design of anode materials based on Nb_2O_5 for sodium-ion devices.[13–15]

A promising strategy used to improve the high C-rate capacity and stability of Nb_2O_5-based electrodes, in both Li- and Na-ion electrolytes, is the combination of the metal oxide with carbon materials, such as amorphous carbon, carbon nanotubes or graphene-related materials.[8,15–18] Significant enhancements of the electrochemical behavior are observed for composites compared to pure niobium oxide, especially in sodium electrolytes.[19–20] Among the carbon materials, 2D rGO is often chosen for the preparation of Nb_2O_5-carbon composites.[8,21–22] For example, more than 80% of published reports on Nb_2O_5-carbon composites employed as anode active materials in Na-ion energy storage systems, correspond to rGO-based materials.[10,15,17,23–24] This is attributed to rGO having a set of favorable properties for electrochemical applications, which include providing electrical conductivity and mechanical stability, as well as acting as a large surface area support to anchor uniformly dispersed metal oxide nanoparticles, preventing their agglomeration.[25] Additionally, rGO is easily obtained by chemical or thermal reduction processes of graphene oxide (GO) that restores at least part of the aromatic carbon network.[26–27] However, studies carried out with carbons as

[a] Dr. X. Han, Dr. P. A. Russo, Dr. N. Goubard-Bretesché, Prof. N. Pinna
Institut für Chemie and IRIS Adlershof, Humboldt-Universität zu Berlin
Brook-Taylor-Str. 2, 12489 Berlin, Germany
E-mail: patricia.russo@hu-berlin.de
nicola.pinna@hu-berlin.de

[b] Dr. C. Triolo, Prof. S. Santangelo
Dipartimento di Ingegneria Civile dell'Energia, dell'Ambiente e dei Materiali (DICEAM)
Università "Mediterranea", 89122 Reggio Calabria, Italy

[**] A previous version of this manuscript has been deposited on a preprint server (DOI: 10.26434/chemrxiv.10274408.v1).

Supporting information for this article is available on the WWW under https://doi.org/10.1002/celc.202000181

anodes in Na-ion batteries have shown that the type of carbon has a strong effect on the sodium storage performance. In particular, structurally disordered and defect-rich amorphous carbons are promising for sodium-ion energy storage.[28–30] While rGO-based composites show promising electrochemical behavior, the lack of studies comparing them with amorphous carbon-based counterparts makes it unclear if efforts to design composites made with amorphous carbon are being neglected in favor of those containing rGO, especially for Na-ion devices, despite amorphous carbon and its composites being generally less expensive and easier to synthesize.

Here, we compare the chemical, physical and electrochemical properties of composites made of T-Nb_2O_5 and rGO (NG*x*, where *x* is the rGO wt.%) or amorphous carbon (NA*x*, where x is the carbon wt.%). Both types of composites were fabricated via the same sol-gel route in acetophenone, followed by thermal treatment at 700 °C under inert atmosphere, the main difference being the source of the carbon component: GO for the NG*x* samples and 1,3,5-triphenylbenzene (TPB) for NA*x*. First, the rGO content was varied in the NG*x* composites to achieve the best energy-storage performance, which was found for NG15. This sample was then compared with the NA15 counterpart. The latter outperformed NG15 as anode active material in all the Li- and Na-ion half-cells and full hybrid supercapacitors devices investigated, owing to the more favorable properties of NA15, such as smaller particle size and more uniform carbon-oxide contact, which are a direct consequence of the use of the organic compound as the carbon source.

2. Results and Discussion

Composites made of Nb_2O_5 and rGO were produced through a nonaqueous synthesis route in acetophenone. The samples were prepared by adding $NbCl_5$ to a suspension of graphene oxide in acetophenone, followed by heating of the mixture at 220 °C for 20 min under microwave irradiation. The products were subsequently annealed at 700 °C under argon flow to reduce the GO, and generate rGO sheets decorated with Nb_2O_5 nanoparticles (Figure 1). Composites with 8 (NG8), 15 (NG15), and 30 (NG30) wt.% of rGO, as determined by thermogravimetric (TG) analysis (Figure S1), were prepared to determine the effect of the rGO content on their physical/chemical properties and electrochemical behavior toward Li^+ and Na^+ insertion/deinsertion. The influence of the amorphous carbon content on the electrochemical performance of the NA*x* materials has been investigated in a previous work.[31]

To confirm that GO was reduced to rGO during the thermal treatment, Fourier-transform infrared spectroscopy (FT-IR) and X-ray photoelectron spectroscopy (XPS) analysis were performed, and the results are shown in Figures S2 and S3 for NG15. The FT-IR spectrum of the sample before annealing displays intense bands, typical of the oxygen-containing functional groups of GO: a broad intense signal between ca. 1400 and 980 cm^{-1} is attributed to the vibration of C–O bonds belonging to various functional groups (carboxylic acid, epoxy, hydroxyl or ketone groups); the band at 1745 cm^{-1} is assigned to carbonyl groups in carboxylic acids.[32–33] A significant reduction in the relative intensity of the signals from the oxygen-containing groups is observed after thermal treatment at 700 °C, suggesting the elimination of a large amount of O-functionalities during the thermal treatment, i.e., the partial reduction of GO. The high resolution C 1s XPS spectra of the NG15 material before and after annealing are shown in Figure S3. The spectra were deconvoluted into four contributions at 284.6, 286.0, 287.3 and 289.3 eV corresponding to C–C, C–O, C=O and O–C=O species, respectively. After thermal treatment, the oxidation degree of GO, as measured by the integrated intensity ratio of the contributions from oxygenated to non-oxygenated C species, $A_{(C-O+C=O+O-C=O)}/A_{(C-C)}$, decreases (from 0.6 to 0.3), further confirming the partial reduction of GO.

The crystal structure of the composites was evaluated by X-ray diffraction (XRD) and micro-Raman analyses (Figure 2a,b).

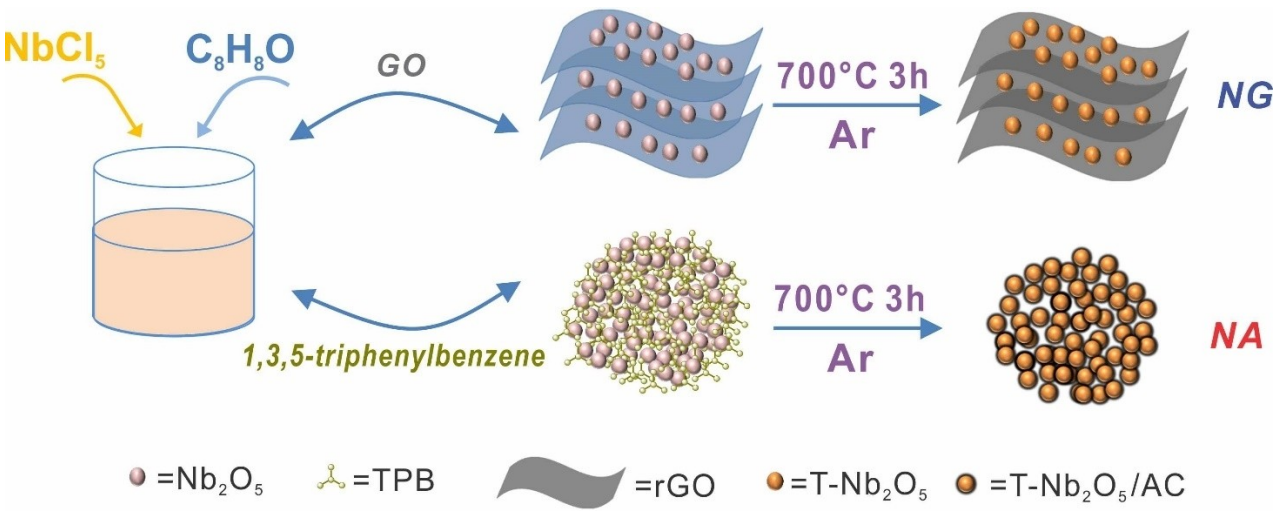

Figure 1. Schematic illustration of the preparation of the Nb_2O_5/rGO (NG*x*) and Nb_2O_5/amorphous carbon (NA*x*) composites

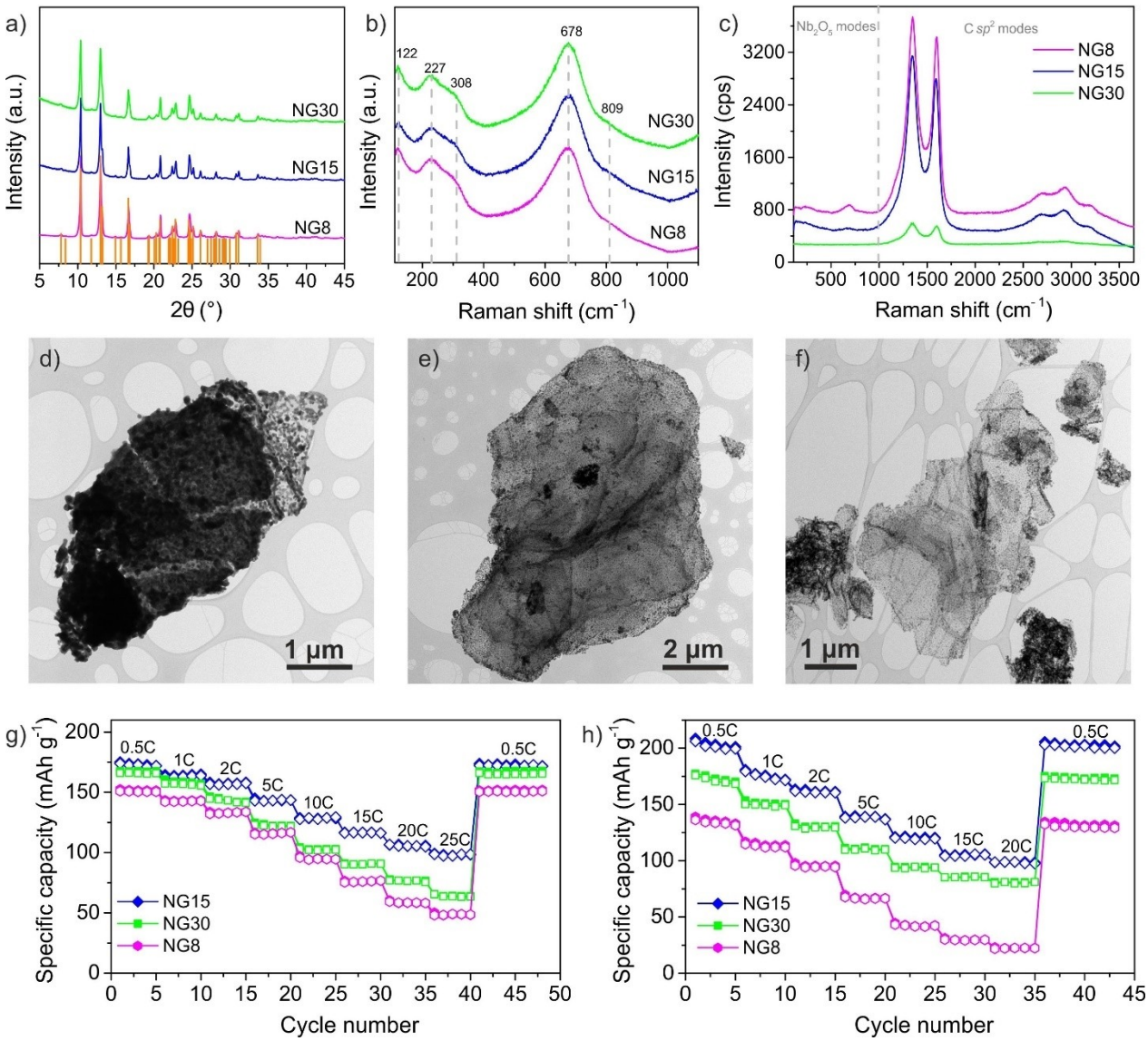

Figure 2. a) XRD patterns (vertical bars correspond to the reference pattern of orthorhombic Nb_2O_5- ICDD file no. 030–0873), b) micro-Raman spectra of the oxide frequency region, and c) as-measured micro-Raman spectra of the NG*x* composites with different rGO contents (8, 15 and 30 wt.%). TEM images of d) NG8, e) NG15 and f) NG30. Specific capacity at various C-rates of the NG*x* samples as anode electrode materials in g) Li-ion half-cells and h) Na-ion half-cells

For all the samples, the reflections are indexed to the orthorhombic phase of niobium pentoxide (T-Nb_2O_5). They are narrow and intense, indicative of the high crystallinity of the oxide in these materials. The results of micro-Raman analysis (Figure 2b) confirm the crystal structure of Nb_2O_5 in the composites. The intense band originating from the symmetrical TO stretch of Nb–O bonds in the T-Nb_2O_5 structural units dominates the oxide phonon mode region ($<1000\ cm^{-1}$) of the spectra.[34–36] It is centered at 678 cm^{-1}, as reported for other T-Nb_2O_5/carbon composites.[34] Its frequency position, down-shifted with respect to the highly crystalline oxide, might be due the formation of oxygen vacancies in the T-Nb_2O_5 crystal structure during the high temperature annealing treatment under argon flow.[37] At higher frequencies ($>1000\ cm^{-1}$), the characteristic bands of graphitic carbons are detected (Figure 2c). The band at 1598 cm^{-1} (G-band) arises from the E_{2g} stretching mode of all sp^2 bonded C=C pairs, whereas the band at 1346 cm^{-1} (for 2.33 eV excitation), originating from the A_{1g} in-plane breathing-mode of the C hexagonal rings, is disorder-activated (D-band).[38] With increasing rGO content, the D/G intensity ratio, calculated as peak amplitude ratios,[38–40] slightly increases (Figure S4a), indicating increased density of the defects in the restored Csp^2 network.[39–40] Conversely, the relative (to G-band) intensity of the main oxide peak progressively weakens (Figure S4b), as expected.

Transmission electron microscopy (TEM) shows that NG8 consists of a thick layer of large oxide nanoparticles (ranging from ~30 to >250 nm) deposited on the rGO (Figure 2d). The large amount of oxide for the rGO surface available led to significant particle coalescence and growth during annealing. NG15 and NG30 (Figure 2e,f) consist of rGO sheets fully decorated with T-Nb_2O_5 nanoparticles (from ~5 to 100 nm),

with a higher density of particles observed for NG15 (Figure 2e,f).

The specific surface area of the samples increases with the increase of the rGO content: 33, 80, and 105 $m^2 g^{-1}$ for NG8, NG15 and NG30, respectively (Figure S5, Table S1). The surface area of NG8 is identical to that of rGO (33 $m^2 g^{-1}$, Table S1), which suggests a dense sandwich type structure, consistent with the TEM observations. All of the composites are mesoporous, with pores of width 5.3 nm, created by the spaces between layers.

To evaluate the energy storage behavior of the materials, Li and Na half-cells were assembled using the NG samples as working electrode materials and metallic lithium or sodium as counter and reference electrodes. The electrochemical performance in the lithium electrolyte was measured within the potential range of 1.0 to 3.0 V (vs. Li/Li^+). The cyclic voltammograms (CVs), galvanostatic charge-discharge (GCD) profiles and C-rate performances are shown in Figures 2g and S6. The insertion/deinsertion of Li^+ to/from the structure of Nb_2O_5 occurs according to the reaction $Nb_2O_5 + xLi^+ + xe^- \leftrightarrow Li_xNb_2O_5$, where x is the molar amount of Li^+ ions inserted (which can reach a maximum of $x = 2$, corresponding to a theoretical capacity of ca. 200 mAh g^{-1}).[6] The CVs of all the three samples exhibit broad anodic and cathodic peaks, which are typical of Nb_2O_5-based nanocomposite materials (Figure S6). Accordingly, the GCD measurements show slopping profiles, which are consistent with the single-phase intercalation mechanism of the Nb_2O_5 material. All of the NG*x*-based electrodes display reversible capacities at the various C-rates studied (from 0.5 C to 25 C), indicative of the high kinetic reversibility of the Li^+ ion intercalation/deintercalation processes. NG8, NG15 and NG30 deliver specific capacities of 150, 173 and 165 mAh g^{-1} at 0.5 C, which decrease to 48, 98 and 63 mAh g^{-1}, respectively, when the rate is increased to 25 C. rGO gives a specific capacity of 17 mAh g^{-1} at 0.5 C that fades rapidly with the increase of the C rate (Figure S7).

The energy-storage behavior of the NG-based electrodes was also evaluated in Na-ion half-cells. The electrochemical measurements were performed in the potential window 0.01 to 3.0 V (vs. Na/Na^+) and the results are shown in Figures 2h and S8. The electrodes exhibit capacity losses above 50% after the first discharge, attributed to the irreversible formation of a solid electrolyte interphase (SEI) and electrolyte decomposition (Figure S8).[14–15] Conversion reactions associated with sodium intercalation/deintercalation take place mainly during the first cycle. After the second cycle, reversible CVs are obtained, with broad contributions attributed to the reaction $Nb_2O_5 + xNa^+ + xe^- \leftrightarrow Na_xNb_2O_5$, indicating the reversibility of the processes after the initial irreversible conversion reactions.

After SEI formation, reversible specific capacities of 134, 202, and 171 mAh g^{-1} at 0.5 C, and 22, 98, and 80 mAh g^{-1} at 20 C, are obtained for NG8, NG15 and NG30, respectively. rGO delivers a capacity of 149 mAh g^{-1} at 0.5 C that decreases to 52 mAh g^{-1} at 10 C in the Na half-cell (Figure S7). Surface reactions have a larger contribution to the total capacity delivered by Nb_2O_5-based electrodes in Na-ion electrolytes compared to Li-ion electrolytes,[7,41] and consequently the electrochemical performance of the samples is linked to their surface area, which is significantly lower for NG8 than for the other nanocomposites.

NG15 shows the best rate performance in both the Li and Na half-cells. The relatively poor electrochemical behavior of NG8 can be attributed to the large Nb_2O_5 particles and dense structure of this material. The smaller oxide particles and the more open structures with higher surface areas of the NG15 and NG30 materials, result in shorter ion/electron transport pathways and easier access of the electrolyte ions to the oxide particles. A 15 wt. % rGO content in the composite provides an optimum balance between the oxide content, the conductivity, increase of surface area arising from the rGO incorporation, and the capacity loss resulting from the lower capacity of the rGO component (especially, for the Li electrolyte). The performance of NG15 is consistent with the results reported in the literature for 2D Nb_2O_5/rGO -based electrodes with similar mass loadings.[10,15,42]

As the NG15 composite exhibits the best rate performance, among the NG*x* samples, in both lithium and sodium electrolytes, its physical, chemical, and electrochemical properties were further compared with those of a composite made of Nb_2O_5 and 15 wt.% of amorphous carbon (NA15). NA15 was synthesized following the same acetophenone route used to produce the NG15 sample, but using a longer reaction time (48 h). The reaction of $NbCl_5$ with acetophenone, for sufficiently long reaction times, generates a mixture of Nb_2O_5 nanoparticles and 1,3,5-triphenylbenzene, which can be annealed under inert atmosphere to produce carbon encapsulated-Nb_2O_5 composites (Figure 1).[31] TPB is formed through condensation of the acetophenone molecules, catalyzed by the Nb_2O_5 itself and HCl (which is a side-product of the oxide formation reaction). Furthermore, TPB can be partially or completely removed from the synthesis product with acetone, allowing the variation of the Nb_2O_5/TPB ratio and consequently of the amount of carbon in the final composite. However, this organic compound is not formed during the short reaction times used to produce the NG15 composite, and thus the carbon component in NG15 derives exclusively from the rGO. The acetophenone route has advantages compared to other approaches for the synthesis of Nb_2O_5 nanoparticles: the carbon source and metal oxide are formed simultaneously in one-step; the amount of TPB surrounding the particles is not limited by the oxide surface available, as it occurs for example with surfactant molecules; the amount of TPB, and thus the amount of carbon in the final material, can be controlled; TPB generates porous carbonaceous materials and therefore leads to less dense carbon coatings compared to other carbon sources such as glucose.[31]

NA15 was prepared by reacting $NbCl_5$ with acetophenone for 48 h followed by thermal treatment of the Nb_2O_5/TPB mixture in the same conditions as those used for synthesizing NG15. To exclude any influence of the reaction time on the characteristics of the niobium oxide, Nb_2O_5 particles produced after 20 min reaction (without addition of GO) and after 48 h reaction (after complete washing of the TPB molecules) were compared. The characterization data shows that the reaction

time has no effect on the properties of the Nb_2O_5 component such as crystallinity or particle size (Figure S9).

The transformation of the TPB molecules during annealing was evaluated by FT-IR (Figure S2). The spectrum of NA15 before thermal treatment is dominated by the bands of TPB. Those bands disappear after thermal treatment, and, instead, two broad signals at ca. 627 and 827 cm^{-1} are observed, which are assigned to the vibrations of Nb–O bonds of the NbO_x polyhedra ($x = 6,7$) in the Nb_2O_5 structure.[43] In addition, the broad band at ca. 1600 cm^{-1} is attributed to carbon and adsorbed water, and the band at 1263 cm^{-1} is assigned to the vibration of C–O bonds of oxygen-containing surface moieties of the carbon. These results indicate the complete transformation of the organic compound during the thermal treatment. Signals associated with TPB are not observed on the spectrum of NG15 before annealing (Figure S2), confirming that the carbon component of NG15 contains only rGO.

The TG curves of the NG15 and NA15 composites reveal that the samples have a similar amount of carbon component in their composition (Figure 3a). However, the carbon in NA15 is less stable under the oxidizing conditions and is completely decomposed at a temperature ca. 100 °C lower than that of the NG15 sample. The higher reactivity toward oxygen suggests the carbon in NA15 has a more amorphous nature compared to rGO. Figure 3b compares the XRD patterns of NG15 and NA15 and shows that the niobium pentoxide in NA15 also has orthorhombic structure. However, the reflections are significantly broader for NA15 than NG15, indicating much smaller T-Nb_2O_5 crystallites in the former. Consistently, all the bands are broader in the Raman spectrum of NA15 (Figure 3c), and those arising from the bending of Nb–O–Nb bonds (at 228 and 308 cm^{-1}) are hardly resolved.[44–45] Besides, the band originating from the vibrations of octahedra as a whole (at 122 cm^{-1})[45] sharpens and a very weak contribution appears at ~985 cm^{-1}. Although the latter spectral changes hint at the presence of a small content of octahedral distortions in the T-Nb_2O_5 nanocrystals due to surface species, such as O=Nb–O with one short O=Nb bond and one elongated Nb–O bond,[35–36] the frequency position of the main band (693 cm^{-1}) is typical of a highly crystalline oxide. The D- and G-bands are located at the same frequencies for NA15 and NG15, indicating comparable oxidation degrees of the carbon in the two types of composites (Figure 3d).[40] The broader bands in the spectrum of the former indicates broader distributions of bond angles and lengths, which is consistent with the more amorphous nature of the carbon, as suggested by TG analysis. As expected, comparable values of the relative (to carbon) oxide intensity are found for the two types of samples with same composition (Figure S4b). The high resolution Nb 3d XPS spectra of NA15 and NG15 show identical features (Figure S10), consisting of a doublet at binding energies of 207.4 eV ($3d_{5/2}$) and 210.2 eV ($3d_{3/2}$) that are typical of niobium with oxidation state 5+ in niobium oxide.[46]

The TEM and high resolution TEM (HRTEM) images (Figure 4) of NA15 show small agglomerates of carbon-encapsulated

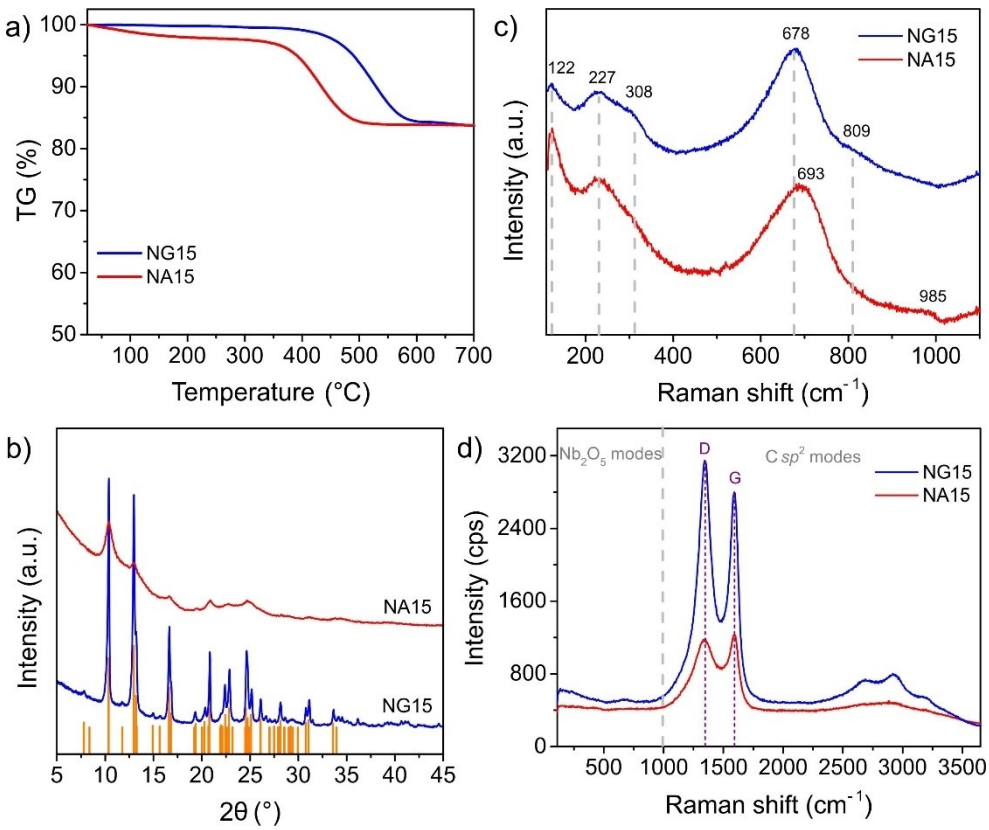

Figure 3. Comparison between the a) TG curves, b) XRD patterns (vertical bars correspond to the reference pattern of orthorhombic Nb_2O_5- ICDD file no. 030-0873), and c, d) micro-Raman spectra of the NG15 and NA15 composites.

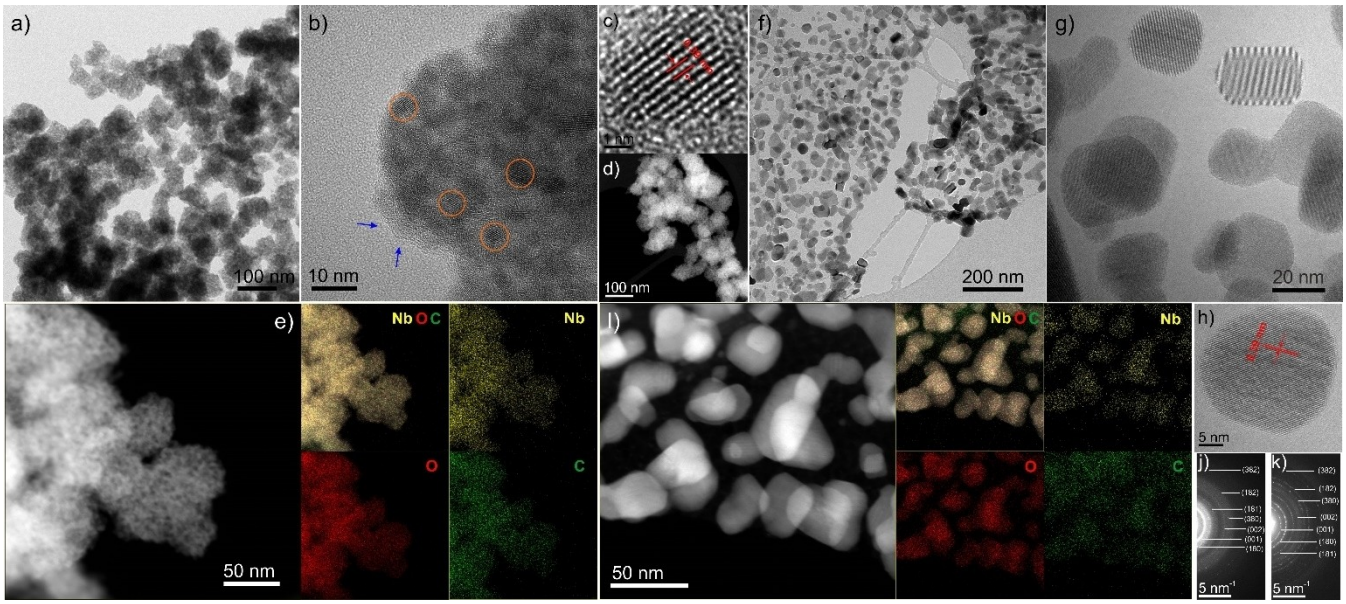

Figure 4. Electron microscopy analysis of the NG15 and NA15 composites: a) TEM, b,c) HRTEM, and d,e) STEM-HAADF images and EDS elemental mapping of NA15; f) TEM, g,h) HRTEM, and i) STEM-HAADF image and corresponding EDS elemental maps of NG15; j,k) SAED patterns of NA15 and NG15, respectively.

Nb_2O_5 nanocrystals of ca. 5 nm. Scanning transmission electron microscopy- high angular annular dark field (STEM-HAADF) imaging indicates the composite is porous (Figure 4d), which was confirmed with nitrogen sorption measurements. NA15 has a specific surface area of 89 $m^2 g^{-1}$ and mesoporosity ranging from 4 to 50 nm, with the maximum of the pore size distribution at 27 nm (Figure S5, Table S1). The porous nature of the material is attributed to the small size of the oxide particles and properties of the carbon surrounding it (as TPB is a monomer of porous polymers). NG15 and NA15 are both mesoporous, have similar surface areas and porous volumes (Table S1). However, NA15 contains much larger porosity (Table S1), which is an important factor affecting the metal-ion storage kinetics.[22,47] The energy dispersive X-ray spectroscopy (EDS) C, Nb, and O elemental maps show a homogeneous distribution of the carbon in the sample (Figure 4e), demonstrating that the oxide nanocrystals are uniformly coated. Despite the same annealing temperature being employed, the Nb_2O_5 particles are larger in NG15 than in NA15, which is explained by the different carbon sources used. Since the TPB molecules completely surround the oxide during the annealing process, they are able to suppress its growth at high temperatures, whereas the ability of GO to suppress the growth of the particles stacked between the 2D sheets is more limited. The EDS C, Nb, and O maps of NG15 hint at the efficient contact between the individual Nb_2O_5 particles and the rGO (Figure 4i). The HRTEM images in Figure 4c,h demonstrate the equally high crystallinity of the orthorhombic Nb_2O_5 nanocrystals in both composites. The selected area electron diffraction (SAED) patterns (Figure 4j,k) further confirm the orthorhombic structure of the Nb_2O_5 in both composites.

The energy storage behavior of NG15 and NA15 as anode electrode materials in the Li and Na electrolytes was compared, first in half-cells and subsequently in full HSC devices. The CVs of the NG15 and NA15 electrodes, measured in the potential range 1.0 to 3.0 V (vs. Li/Li^+) at different sweep rates, exhibit broad cathodic and anodic peaks associated with the insertion/deinsertion of Li^+ ions to/from the T-Nb_2O_5 structure (Figure 5 a,b). The peaks are slightly broader for the NA15 electrode, which is attributed to the smaller size of the oxide particles. The first five GCD curves show in both cases a small initial irreversible capacity loss caused by side-reactions associated with the formation of a SEI, after which the capacity reaches constant values that reflect the reversibility of the charge-discharge processes for both materials (Figures S6 and S11). Figure 5e compares the C-rate performance of the composites, revealing that NA15 delivers a higher capacity than NG15 at all the C rates. Specifically, NA15 gives a specific capacity of 189 mAh g^{-1} at 0.5 C against 173 mAh g^{-1} for NG15, and 134 mAh g^{-1} against 98 mAh g^{-1} at 25 C. The specific capacities of the carbon in the Li- and Na-ion electrolytes are shown in Figure S7. These results suggest that faster electron and ion transport occurs for NA15. It is worth mentioning that a composite containing 10 wt. % of amorphous carbon (NA10) further outperforms NG15, exhibiting a capacity of 192 mAh g^{-1} at 0.5 C and 159 mAh g^{-1} at 25 C (Figure S12). Electrochemical impedance spectroscopy (EIS) measurements were carried out and the Nyquist plots recorded after 100 cycles are compared in Figure S13. The radius of the semicircle in the high-frequency region of the plots, which is associated with the electrode charge-transfer process, is smaller for the NA15 electrode. This means that the charge-transfer resistance at the electrode-electrolyte interface is lower for NA15, allowing faster electron and ion transport, which is consistent with the enhanced rate capability. The superior rate performance of NA15 is ascribed, on the one hand, to the homogeneous coating of the oxide

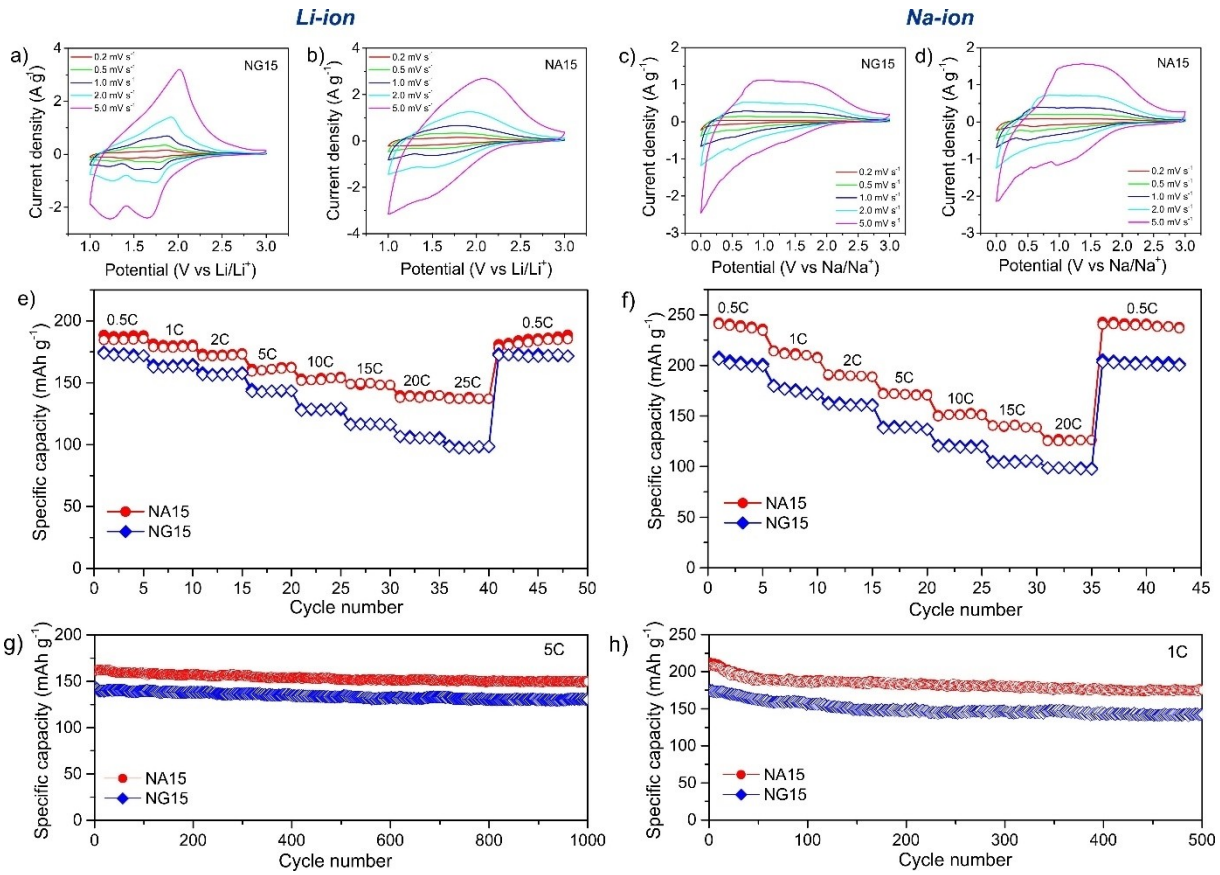

Figure 5. Comparison between the electrochemical performance of the NG15 and NA15 composites in the Li- and Na-ion half-cells: a,b,c,d) cyclic voltammograms at different sweep rates, e,f) specific capacities at various C-rates, and g,h) cycling stability at 5 C (Li-ion) and 1 C (Na-ion).

particles that leads to an intimate contact between the entire oxide surface and the amorphous carbon, which, contrary to the nanoparticles supported on rGO, promotes a more efficient electron and ion transport. On the other hand, the smaller oxide particles in NA15 result in shorter ion-diffusion paths for Li insertion/deinsertion, contributing to the higher capacity and rate capability of NA15. In addition, the larger porosity and more open structure of NA15 also facilitates ion transport and leads to faster kinetics. No superiority in terms of stability is observed for the rGO-based composite compared with the amorphous carbon-based material. Both electrodes are similarly stable, being able to maintain ca. 87% of their initial capacities after 1000 charge-discharge cycles at 5 C (Figure 5g).

The energy storage performances of NG15 and NA15 in sodium half-cells, measured in the potential window 0.01 to 3 V (vs. Na/Na^+), are shown in Figures 5 and S11. The GCD curves at 0.25 C exhibit capacity losses of ca. 51% for both electrodes after the first discharge due to SEI formation (Figures S8 and S11), and after the second cycle reversible capacities of 255 mAh g^{-1} for NG15 and 271 mAh g^{-1} for NA15 are attained. The CVs measured at sweep rates between 0.2 and 5 mV s^{-1} (Figure 5c,d), after SEI formation, are reversible and display broad peaks caused by sodium intercalation/deintercalation. As observed for the Li half-cell, NA15 delivers higher capacities at all the C-rates. NA15 gives a specific capacity of 237 mAh g^{-1} at 0.5 C compared to 202 mAh g^{-1} for NG15 and sustains a high capacity of 125 mAh g^{-1} at 20 C compared to 98 mAh g^{-1} for NG15. The surface areas do not play a major role in the different Na storage performances of the composites, since they are similar (80 and 89 $m^2 g^{-1}$ for NG15 and NA15, respectively). Therefore, as found for the lithium system, the superior capacity of NA15 is caused by shorter pathways for ion and electron transport, more homogeneous carbon-oxide contacts, and larger porosity, which promote faster electron and ion transport. The NG15 electrode maintains a stable performance up to 500 charge-discharge cycles at 1 C rate (Figure 5h), after an initial capacity loss of 15% during the first 100 cycles (due to irreversible conversion reactions). The stability of NG15 in the Na electrolyte is therefore comparable to that of NA15, demonstrating that the combination of Nb_2O_5 with rGO does not lead to any additional stability improvement.

The NG15 and NA15 electrodes were further employed as anode electrode materials in hybrid supercapacitor devices, including Li-ion (LICs) and Na-ion (NICs) cells (Figures S14–S16). Commercial activated carbon (YPF-50) was used at the cathode, and the mass ratio between the anode and cathode used for constructing the HSC devices was 1:3.5. The CVs of the NG15 and NA15 LICs, measured in the potential window of 0.5 to 3.5 V at sweep rates from 0.5 to 10 mV s^{-1}, are shown in Figure S14. The shape of the CVs is a combination of the

faradaic and non-faradaic storage processes occurring at the anode and cathode, respectively. The galvanostatic charge-discharge curves were measured at current densities between 0.1 and 1.0 $A g^{-1}$ (Figure S14).

All of the curves show quasi-triangular shapes that agree with the CV data and are typical of such hybrid devices. Both materials are able to retain around 89% of their initial energy density after 2000 cycles at 1 $A g^{-1}$ and operate with a coulombic efficiency close to 100%. However, the CVs of NG15 show smaller integral areas at the same scan rate compared to those of NA15 and the galvanostatic charge-discharge curves indicate slightly lower discharge time at the same current density, which reflects a lower energy storage capacity for NG15 compared to NA15 and is consistent with the results obtained in the half-cells. The energy density (*E*) and power density (*P*) of the devices are compared in the Ragone plot displayed in Figure S16, which demonstrates that the NA15 LIC delivers higher maximum *E* and *P* than the NG15 LIC. It is worth mentioning that the performance of both the LIC and NIC hybrid supercapacitors is poor compared to some literature data. This is because the performance of these devices depends also on the cathode chosen and mass ratio between anode and cathode, which needs to be optimized. However, in this work we were only interested in comparing the NG15 and NA15 composites as anode electrodes. The CVs of the NICs based on NG15 and NA15, measured in the voltage window of 1.0-4.3 V at various sweep rates, are shown in Figure S15. All of the curves deviate from the rectangular shape typical of capacitors due to the combination of the faradaic pseudocapacitive intercalation process and capacitive physisorption process. The galvanostatic charge-discharge curves of both NIC devices at different current densities reveal a similar quasi-symmetric triangular shape (Figure S15). The area delimited by the CVs of NA15 is significantly larger than that of NG15 at the same scan rate, indicating that the energy storage capacity of NA15 is higher than that of NG15. This is also supported by comparing the galvanostatic charge-discharge curves at the same current density, which show that the discharge time is higher for NA15 than for NG15. Both NIC devices exhibit good cycle stability, with nearly 100% coulombic efficiency and a capacitance retention of 86% after 1200 cycles at a current density of 1 $A g^{-1}$ (Figure S15). The NIC device assembled with NG15 delivers a maximum *E* of 58.5 $Wh kg^{-1}$ at *P* of 50 $W kg^{-1}$. This NIC device exhibits lower power and energy density than the NA15-based NIC (Figure S16). These results are in full agreement with the half-cell measurements and further confirm the superiority of the NA15 composite for Li and Na storage systems.

3. Conclusions

Composites made of orthorhombic Nb_2O_5 NCs and rGO (ranging from 8 to 30 wt. %) were produced via reaction of $NbCl_5$ with acetophenone in the presence of GO, followed by annealing. Among the samples, NG15 (containing 15 wt. % rGO) exhibited enhanced high rate performance as anode electrode material in both Li and Na half-cells, achieving a specific capacity of 98 $mAh g^{-1}$ at 25 C (for Li) and 20 C (for Na). For comparison, a composite consisting of Nb_2O_5 NCs and 15 wt. % of amorphous carbon (NA15) was synthesized through the same reaction in acetophenone, but instead using 1,3,5-triphenylbenzene as carbon source. NA15 delivered specific capacities of 134 $mAh g^{-1}$ at 25 C (for Li) and 125 $mAh g^{-1}$ at 20 C (for Na) in the half-cells. The HSC devices constructed with NA15 at the anode also outperformed those of NG15, delivering higher energy densities and power densities in both Li and Na electrolytes, while showing comparable cyclabilities. The superior rate behavior of NA15 is attributed to the homogeneous and intimate contact between the entire surface of the oxide particles and the carbon, to the small size of the oxide NCs, and to the larger porosity, which facilitate the electron and/or ion transport. Those composite properties are a consequence of using the organic molecule homogeneously surrounding the oxide particles as the carbon source, which simultaneously limits the oxide growth during annealing, leads to an uniform carbon coating, and creates porosity. The results reported here demonstrate that composites of metal oxide with amorphous carbon can have advantageous properties for energy storage compared to those based on rGO.

Experimental Section

Synthesis

Graphene oxide (10, 25 or 50 mg, to obtain NG8, NG15 and NG30, respectively) was first dispersed in 20 mL of acetophenone in a 30 mL microwave glass vial under argon through sonication. Niobium (V) chloride (0.135 g) was then added to the suspension in a glovebox under argon, and the mixture was stirred to dissolve the niobium precursor. The vial was sealed with a silicone cap and subsequently heated in a microwave reactor at 220 °C for 20 min (with a 5 min heating ramp to reach the final temperature). After rapidly cooling the reaction mixture with compressed air, the product was collected by centrifugation, washed with ethanol followed by acetone, and dried at 70 °C. The resulting Nb_2O_5/GO sample was thermally treated in a tubular oven under argon flow at 700 °C for 3 h, with a heating rate of 10 °C min^{-1}. GO was synthesized from graphite powder following a modified Hummers' method, as previously described.[48–49]

To synthesize the NA15 composite, niobium (V) chloride (0.135 g) was dissolved in 20 mL of acetophenone in a glovebox under argon, and the solution was transferred to a Teflon-lined stainless-steel autoclave, and then heated at 220 °C for 48 h. The product was collected by centrifugation, washed with ethanol, and dried at 70 °C. The resulting inorganic-organic mixture was thermally treated under argon flow at 700 °C for 3 h, with a heating rate of 10 °C min^{-1}.

Characterization

X-ray diffraction (XRD) patterns were recorded with a STOE MP diffractometer in transmission configuration using Mo K_α radiation ($\lambda = 0.07093$ nm). Transmission electron microscopy (TEM) and high resolution TEM (HRTEM) images were acquired on a Philips CM 200 and FEI Talos 200S microscope operated at 200 kV. A NT-MDT NTEGRA – Spectra SPM spectrometer, equipped with MS3504i

350 mm monochromator and ANDOR Idus CCD, was utilized to measure Raman scattering, excited by a solid-state laser operating at 2.33 eV (532 nm). The scattered light from the sample was dispersed by an 1800 lines/mm grating and collected by a Mitutoyo high numerical aperture 100X objective. In order to obtain a sufficiently high signal-to-noise ratio in the region of the Nb_2O_5 phonon modes, a laser power of 740 μW at the sample surface was utilized. Lower resolution spectra were further recorded, by the use of a 600 lines/mm grating, to analyze the region of the Csp^2 phonon modes ($>1000\ cm^{-1}$). In order to prevent structural damage of the carbon coating induced by local heating, these spectra were recorded by utilizing a very low laser power (110 μW at the sample surface). Finally, in order to have a reliable picture of their bulk, spectra from several random positions on each specimen were collected. The spectra were then averaged and quantitatively analyzed. X-ray photoelectron spectroscopy (XPS) measurements were performed using a Thermo Fischer Scientific ESCALAB 250Xi instrument, with an Al K_α source, in constant analyzer energy mode with a pass energy of 50 eV and a spot size of 400 μm. A NETZSCH thermoanalyzer STA 409 C Skimmer system, equipped with BALZERS QMG 421, was used to record the thermoanalytical curves. A synthetic air flow of 70 mL min^{-1} and a heating rate of 10 °C min^{-1} were applied. Nitrogen sorption isotherms at −196 °C were acquired on a Micromeritics ASAP 2020, after degassing the solids at 200 °C overnight.

Electrochemical measurements

The Nb_2O_5 working electrodes were prepared by homogeneously mixing active materials, carbon black (super C 65) and polyvinylidene fluoride (70:20:10 by weight) in N-methyl-2-pyrrolidinone (NMP). Then, the obtained slurries were coated on copper foil and spread with a doctor blade apparatus for a thickness of 250 μm (not including the Cu foil), and subsequently dried at 70 °C for 1 h. The dried electrodes were cold-laminated and punched into 18-mm diameter discs that were dried at 120 °C overnight in a Büchi vacuum oven, before being transferred to an Ar-filled glovebox for coin-cell assembly. The mass loading of all active materials was controlled within the range of 1.1–1.5 mg cm^{-2} so that meaningful comparisons between the samples could be made. Both half-cell and full-cell electrochemical measurements were carried out using 2032-type coin cells. Half-cells were assembled using Nb_2O_5 as the working electrode material and metallic lithium (or sodium) as both counter and reference electrodes. For lithium-based half-cells, 1.0 M $LiPF_6$ in ethylene carbonate : diethyl carbonate : dimethyl carbonate (EC:DEC:DMC, 1:1:1 vol. ratio) was used as electrolyte, whereas a 1 M $NaClO_4$ solution in ethylene carbonate : propylene carbonate : fluoroethylene carbonate (EC:PC:FEC, 48:48:4 vol. ratio) was used for Na-ion systems. In both cases, a glass fiber filter (Whatman) served as a separator. Full-cells were assembled using Nb_2O_5-based electrodes as anodes and activated carbon (AC) as a cathode material, in the corresponding Li-ion or Na-ion electrolyte. The AC electrodes were prepared by thoroughly mixing commercial activated carbon (YPF-50, Kuraray), carbon black (Super C65) and polyvinylidene fluoride (80:10:10 by weight) in NMP. The prepared slurries were coated on an aluminum foil. All the subsequent steps were the same as for the Nb_2O_5-based electrodes. Prior to assembling the full cells, the niobium oxide electrodes were pre-lithiated or pre-sodiated. The weight ratio of the active materials in the cells was balanced to be 1:3.5 in a voltage window of 0.5–3.5 V for the Li-ion capacitor and 1.0–4.3 V for its sodium counterpart. Cyclic voltammetry (CV) was performed at various scan rates with a Bio-Logic VMP3 potentiostat/galvanostat and the galvanostatic charge/discharge (GCD) tests were carried out at different C-rates, using a LAND electrochemical workstation (Wuhan). In half-cells, the specific capacity values were calculated according to the total mass of the Nb_2O_5-based composites, including carbon. In full-cell configuration, the total mass of active materials (in both anode and cathode) was taken into account. The energy and power density values of the full-cells were calculated from the GCD results, using the equations: $E = \int_{t1}^{t2} IV(t)dt$ and $P = \frac{E}{t}$, where I is the current density applied during the electrochemical measurement, in A kg^{-1} based on the total mass of the active materials in both electrodes, V is the working voltage during the discharging process (in V), and t is the discharging time (in h). Electrochemical impedance spectroscopy (EIS) was performed at open circuit potential (OCP) in half-cell configuration, by sweeping frequencies from 100 kHz to 10 mHz with an amplitude of 10 mV.

Acknowledgements

X.H. acknowledges the fellowship from the China Scholarship Council (CSC). P.A.R. acknowledges the support from the DFG (RU2012/2-1). S.S. gratefully thanks the Italian Ministry of Education, University and Research (MIUR) for the partial financial support through the PRIN project 2017MCEEY4, TRUST (Towards sustainable, high-performing, all-solid-state sodium-ion batteries). The authors thank C. Erdmann for performing the electron microscopy measurements.

Conflict of Interest

The authors declare no conflict of interest.

Keywords: Nb_2O_5 · amorphous carbon · reduced graphene oxide · Li-ion storage · Na-ion storage

[1] P. Simon, Y. Gogotsi, B. Dunn, *Science* **2014**, *343*, 1210–1211.
[2] M. D. Slater, D. Kim, E. Lee, C. S. Johnson, *Adv. Funct. Mater.* **2013**, *23*, 947–958.
[3] W. Zuo, R. Li, C. Zhou, Y. Li, J. Xia, J. Liu, *Adv. Sci.* **2017**, *4*, 1600539.
[4] V. Augustyn, P. Simon, B. Dunn, *Energy Environ. Sci.* **2014**, *7*, 1597–1614.
[5] V. Aravindan, J. Gnanaraj, Y.-S. Lee, S. Madhavi, *Chem. Rev.* **2014**, *114*, 11619–11635.
[6] V. Augustyn, J. Come, M. A. Lowe, J. W. Kim, P.-L. Taberna, S. H. Tolbert, H. D. Abruña, P. Simon, B. Dunn, *Nat. Mater.* **2013**, *12*, 518–522.
[7] J. W. Kim, V. Augustyn, B. Dunn, *Adv. Energy Mater.* **2012**, *2*, 141–148.
[8] X. Wang, G. Li, Z. Chen, V. Augustyn, X. Ma, G. Wang, B. Dunn, Y. Lu, *Adv. Energy Mater.* **2011**, *1*, 1089–1093.
[9] N. Kumagai, I. Ishiyama, K. Tanno, *J. Power Sources* **1987**, *20*, 193–198.
[10] L. Wang, X. Bi, S. Yang, *Adv. Mater.* **2016**, *28*, 7672–7679.
[11] L. Yang, Y.-E. Zhu, J. Sheng, F. Li, B. Tang, Y. Zhang, Z. Zhou, *Small* **2017**, *13*, 1702588.
[12] H. Yang, R. Xu, Y. Gong, Y. Yao, L. Gu, Y. Yu, *Nano Energy* **2018**, *48*, 448–455.
[13] Y. Li, H. Wang, L. Wang, Z. Mao, R. Wang, B. He, Y. Gong, X. Hu, *Small* **2019**, 15, 1804539.
[14] J. Ni, W. Wang, C. Wu, H. Liang, J. Maier, Y. Yu, L. Li, *Adv. Mater.* **2017**, *29*, 1605607.
[15] E. Lim, C. Jo, H. Kim, M.-H. Kim, J. Chun, H. Kim, J. Park, K. Roh, K. Kang, S. Yoon, J. Lee, *Adv. Funct. Mater.* **2016**, *26*, 3711–3719.
[16] E. Lim, C. Jo, H. Kim, M.-H. Kim, Y. Mun, J. Chun, Y. Ye, J. Hwang, K.-S. Ha, K. C. Roh, K. Kang, S. Yoon, J. Lee, *ACS Nano* **2015**, *9*, 7497–7505.
[17] L. Yan, G. Chen, S. Sarker, S. Richins, H. Wang, W. Xu, X. Rui, H. Luo, *ACS Appl. Mater. Interfaces* **2016**, *8*, 22213–22219.
[18] G. Ma, K. Li, Y. Li, B. Gao, T. Ding, Q. Zhong, J. Su, L. Gong, J. Chen, L. Yuan, *ChemElectroChem* **2016**, *3*, 1360–1368.

[19] S. Li, T. Wang, W. Zhu, J. Lian, Y. Huang, Y.-Y. Yu, J. Qiu, Y. Zhao, Y.-C. Yong, H. Li, *J. Mater. Chem. A* **2019**, *7*, 693–703.
[20] X. Wang, Q. Li, L. Zhang, Z. Hu, L. Yu, T. Jiang, C. Lu, C. Yan, J. Sun, Z. Liu, *Adv. Mater.* **2018**, *30*, 1800963.
[21] H. Yu, L. Xu, H. Wang, H. Jiang, C. Li, *Electrochim. Acta* **2019**, *295*, 829–834.
[22] H. Sun, L. Mei, J. Liang, Z. Zhao, C. Lee, H. Fei, M. Ding, J. Lau, M. Li, C. Wang, *Science* **2017**, *356*, 599–604.
[23] L. Kong, C. Zhang, J. Wang, W. Qiao, L. Ling, D. Long, *ACS Nano* **2015**, *9*, 11200–11208.
[24] F. Liu, X. Cheng, R. Xu, Y. Wu, Y. Jiang, Y. Yu, *Adv. Funct. Mater.* **2018**, *28*, 1800394.
[25] S. Yang, X. Feng, S. Ivanovici, K. Müllen, *Angew. Chem. Int. Ed.* **2010**, *49*, 8408–8411; *Angew. Chem.* **2010**, *122*, 8586–8589.
[26] C. Gómez-Navarro, R. T. Weitz, A. M. Bittner, M. Scolari, A. Mews, M. Burghard, K. Kern, *Nano Lett.* **2007**, *7*, 3499–3503.
[27] S. Pei, H.-M. Cheng, *Carbon* **2012**, *50*, 3210–3228.
[28] D. A. Stevens, J. R. Dahn, *J. Electrochem. Soc.* 2001, 148, A803.
[29] B. Yang, J. Chen, S. Lei, R. Guo, H. Li, S. Shi, X. Yan, *Adv. Energy Mater.* **2018**, 8, 1702409.
[30] R. H. DeBlock, J. S. Ko, M. B. Sassin, A. N. Hoffmaster, B. S. Dunn, D. R. Rolison, J. W. Long, *Energy Storage Mater.* **2019**, 21, 481–486.
[31] X. Han, P. A. Russo, N. Goubard-Bretesché, S. Patanè, S. Santangelo, R. Zhang, N. Pinna, *Adv. Energy Mater.* **2019**, 9, 1902813.
[32] W. Chen, L. Yan, P. R. Bangal, *Carbon* **2010**, *48*, 1146–1152.
[33] D. R. Dreyer, S. Park, C. W. Bielawski, R. S. Ruoff, *Chem. Soc. Rev.* **2010**, *39*, 228–240.
[34] J. Lin, Y. Yuan, Q. Su, A. Pan, S. Dinesh, C. Peng, G. Cao, S. Liang, *Electrochim. Acta* **2018**, *292*, 63–71.
[35] D. Chen, J.-H. Wang, T.-F. Chou, B. Zhao, M. A. El-Sayed, M. Liu, *J. Am. Chem. Soc.* **2017**, *139*, 7071–7081.
[36] K. Kim, S.-G. Woo, Y. N. Jo, J. Lee, J.-H. Kim, *Electrochim. Acta* **2017**, *240*, 316–322.
[37] W. Zhao, W. Zhao, G. Zhu, T. Lin, F. Xu, F. Huang, *Dalton Trans.* **2016**, *45*, 3888–3894.
[38] A. C. Ferrari, J. Robertson, *Phys. Rev. B* **2000**, *61*, 14095–14107.
[39] L. G. Cançado, A. Jorio, E. H. M. Ferreira, F. Stavale, C. A. Achete, R. B. Capaz, M. V. O. Moutinho, A. Lombardo, T. S. Kulmala, A. C. Ferrari, *Nano Lett.* **2011**, *11*, 3190–3196.
[40] S. Santangelo, *Surf. Interface Anal.* **2016**, *48*, 17–25.
[41] H. Kim, E. Lim, C. Jo, G. Yoon, J. Hwang, S. Jeong, J. Lee, K. Kang, *Nano Energy* **2015**, *16*, 62–70.
[42] Y. Zhao, C. Ding, Y. Hao, X. Zhai, C. Wang, Y. Li, J. Li, H. Jin, *ACS Appl. Mater. Interfaces* **2018**, *10*, 27106–27115.
[43] M. Ristić, S. Popović, S. Musić, *Mater. Lett.* **2004**, *58*, 2658–2663.
[44] G. Falk, M. Borlaf, M. J. López-Muñoz, J. C. Fariñas, J. B. Rodrigues Neto, R. Moreno, *J. Mater. Res.* **2017**, *32*, 3271–3278.
[45] L. Kong, C. Zhang, J. Wang, W. Qiao, L. Ling, D. Long, *Sci. Rep.* **2016**, *6*, 21177.
[46] S. Liu, J. Zhou, Z. Cai, G. Fang, Y. Cai, A. Pan, S. Liang, *J. Mater. Chem. A* **2016**, *4*, 17838–17847.
[47] C.-H. Lai, D. Ashby, M. Moz, Y. Gogotsi, L. Pilon, B. Dunn, *Langmuir* **2017**, 33, 9407–9415.
[48] W. S. Hummers Jr, R. E. Offeman, *J. Am. Chem. Soc.* **1958**, *80*, 1339–1339.
[49] P. A. Russo, N. Donato, S. G. Leonardi, S. Baek, D. E. Conte, G. Neri, N. Pinna, *Angew. Chem. Int. Ed.* **2012**, *51*, 11053–11057; *Angew. Chem.* **2012**, *124*, 11215–11219.

Manuscript received: February 4, 2020
Accepted manuscript online: March 22, 2020